

# NJC

New Journal of Chemistry

Accepted Manuscript

A journal for new directions in chemistry

This article can be cited before page numbers have been issued, to do this please use: S. Ikram, M. Müller, S. Dsoke, U. A. Rana, A. Sarapulova, W. Bauer, H. M. Siddiqi and D. V. V. Szabó, *New J. Chem.*, 2019, DOI: 10.1039/C9NJ02488C.



This is an Accepted Manuscript, which has been through the Royal Society of Chemistry peer review process and has been accepted for publication.

Accepted Manuscripts are published online shortly after acceptance, before technical editing, formatting and proof reading. Using this free service, authors can make their results available to the community, in citable form, before we publish the edited article. We will replace this Accepted Manuscript with the edited and formatted Advance Article as soon as it is available.

You can find more information about Accepted Manuscripts in the [Information for Authors](#).

Please note that technical editing may introduce minor changes to the text and/or graphics, which may alter content. The journal's standard [Terms & Conditions](#) and the [Ethical guidelines](#) still apply. In no event shall the Royal Society of Chemistry be held responsible for any errors or omissions in this Accepted Manuscript or any consequences arising from the use of any information it contains.

## ARTICLE

# One step *in situ* synthesis of ZnS/N and S Co-doped Carbon Composites *via* salt templating for Lithium-ion battery application

Received 00th January 20xx,  
Accepted 00th January 20xx

DOI: 10.1039/x0xx00000x

Sadaf Ikram<sup>a,b</sup>, Marcus Müller<sup>b</sup>, Sonia Dsoke<sup>b,c</sup>, Usman Ali Rana<sup>d</sup>, Angelina Sarapulova<sup>b</sup>, Werner Bauer<sup>b\*</sup>, Humaira M. Siddiqi<sup>a\*</sup>, Dorothée Vinga Szabó<sup>b,e</sup>

Herein, we report a simple *in situ* synthetic route to prepare ZnS/Carbon composites (ZnS/NSC-x) by using an eutectic salt mixture (LiCl/ZnCl<sub>2</sub>) as a template and 2-amino-4-phenyl thiazole as a precursor for carbon material. The structural and morphological characterization reveals the presence of cubic ZnS (9nm) nanoparticles embedded in the carbon material. These synthesized heteroatom co-doped composites (ZnS/NSC-x) with moderate surface area, used as the positive electrode in a lithium-ion battery, gave better performance than pure ZnS both in terms of cycling stability and rate performance. The capacity retention at the high current density of 1500 mA g<sup>-1</sup> is 65% respect to the capacity obtained at 250 mA g<sup>-1</sup> for ZnS/NSC-800, whereas pure ZnS retained only the 28% of capacity at same current density. The charge transfer resistance values are also found to be very low for the synthesized composites which are responsible for their improved kinetics. The heteroatom co-doped carbon matrix besides improving the electronic conductivity also relieved the stress induced by cycling, therefore the electrode with high mass loading of up to 4 mg cm<sup>-2</sup> gave stable capacity with 90% of the initial capacity, over 200 cycles (at 250 mA g<sup>-1</sup>) for the same electrode at which the rate performance was carried out.

## 1. Introduction

Lithium-ion batteries (LIBs) are popular rechargeable batteries, which can store twice the energy stored by other technologies like nickel and lead batteries<sup>1</sup>. The most common commercial anode material used in LIBs is graphitic carbon, which has good cyclic stability and relatively low cost. However, graphite suffers from a low theoretical capacity (375 mAh g<sup>-1</sup>), which brings obvious consequences in terms of energy density<sup>2-4</sup>.

Therefore, in order to fulfill the growing energy demand and to meet the requirements for large-scale productions, there is a need to explore novel high capacity anode materials. In this context, various transition metal oxides (MnO, SnO<sub>2</sub>, CuO, NiO, Fe<sub>3</sub>O<sub>4</sub>, ZnO, Co<sub>3</sub>O<sub>4</sub>, Ni<sub>2</sub>CoO<sub>4</sub> etc) and metal sulfides (such as NiS, FeS, ZnS, Co<sub>9</sub>S<sub>8</sub>, NiCoS etc) have gained much attention because of their high natural abundance, high theoretical specific capacity and non-toxic nature<sup>5-7</sup>. However, in comparison to metal oxides, the transition metal sulfides have proven to be a better choice due to their better electrical conductivity and the large specific capacity. In addition, the weaker metal-sulfur bond makes the conversion reactions of metal sulfides kinetically more favored than those of metal oxides<sup>8-10</sup>.

Among several metal sulfides, ZnS attracted considerable attention because of its easy synthesis, low cost, non-toxicity, and high theoretical capacity (962 mAh/g), but the practical application of ZnS is hindered due to its poor electrical conductivity and large volume change during cycling<sup>11</sup>. As the Li insertion/extraction mechanism on ZnS involves conversion and alloying reactions during Li insertion/extraction, it suffers from rapid expansion/shrinkage. This dramatic change in volume results into the loss of electrical contact from the collector foil, thus causing a rapid capacity fading. Moreover,

\*a. Department of Chemistry, Quaid-i-Azam University, Islamabad, Pakistan, 45320

\*b. Institute for Applied Materials, Karlsruhe Institute of Technology, Hermann-von-Helmholtz-Platz 1, D-76344, Eggenstein-Leopoldshafen, Germany

c. Helmholtz-Institute Ulm for Electrochemical Energy Storage (HIU), P.O. Box 3640, D-76021 Karlsruhe, Germany

d. Sustainable Energy Technologies (SET) centre, college of engineering, PO-Box 800, King Saud University, Riyadh 11421, Saudi Arabia

e. Karlsruhe Nano Micro Facility (KNMF), Karlsruhe Institute of Technology, Hermann-von-Helmholtz-Platz 1, D-76344, Eggenstein-Leopoldshafen, Germany

\*Corresponding authors: werner.bauer@kit.edu (W. Bauer); humairas@qau.edu.pk (Humaira M. Siddiqi)

poor electronic conductivity is also responsible for its poor rate performance<sup>12, 13</sup>.

To address these problems, various strategies have been devised. One of the strategies is to reduce the ZnS particle size to the nanoscale as this shortens the transport pathways for ion and electrons movement, thus facilitating the charge storage process at high current rates and improving the rate capability<sup>14, 15</sup>. Nevertheless, nanosizing also increases the interface exposure to an electrolyte, resulting in excessive solid electrolyte interphase (SEI) formation. In another approach, to alleviate the poor conductivity and electrode pulverization problem, hybridization of ZnS with the variety of nanostructured carbonaceous materials including graphene, reduced graphene oxide, carbon nanotubes, and micro/mesoporous carbons, etc. has been done<sup>3, 16-18</sup>.

In this respect amorphous porous carbon-based composites also provide extra storage sites but at the expense of poor conductivity due to less graphitization. So to overcome this problem heteroatom doping (such as N, P, S or B) has been proven beneficial as it improves the electronic structure by shifting the Fermi level to the valence or conduction band<sup>19, 20</sup>. N and S are the extensively studied dopants; N doping improves the electronic conductivity and S because of its large size increase interlayer spacing which creates micropores for ion storage. Moreover, its polarizable lone pairs can change the adjacent carbon charge state which improves the adsorption ability. Importantly when these interactive heteroatoms are co-doped their synergistic effects can be generated which is helpful in improving electrochemical stability<sup>21-23</sup>.

Mostly, the ZnS composites have been prepared by first synthesizing ZnS and then applying a carbon coating with various precursors such as glucose, polydopamine, etc.<sup>24</sup>. Li et al<sup>24</sup> prepared ZnS/Nitrogen-doped composite by following the same strategy using polydopamine as a source of nitrogen doped carbon coating. Metal-organic frameworks (MOFs) have also been used as precursors for the synthesis of ZnS/Carbon Composites. Fu et al<sup>12</sup> prepared nitrogen doped porous carbon from MOFs that displays a capacity of 438 mAh/g at a current density of 0.1A/g after 100 cycles. The introduction of various heteroatoms (N, S, etc.), beneficial for improving the carbon conductivity, involves extra nitrogen and sulfur sources like thiourea, urea, 2-amino thiophenol, etc.<sup>25</sup>. The previous studies focused on the synthesis of composites, where the extra carbonaceous material and the heteroatoms are added in a different step. Additionally, the activation of carbon material (necessary to increase the surface area) also requires another step. Hence all these methods involve multistep and complex synthetic procedures. Moreover, the addition of carbonaceous agents afterward also leads to poor connectivity of ZnS with the carbon framework.

In the present work, we have devised a novel strategy for facile one step *in situ* synthesis of ZnS/NSC-x composites *via* salt templating method. Salt templating has been proven as an effective method for controlling the microstructure of carbonaceous materials. These templates can be easily removed after carbonization by subsequent washing with

distilled water<sup>26</sup>. Here for the first time, we have used a eutectic mixture (LiCl/ZnCl<sub>2</sub>) as a template to prepare the porous ZnS/NSC-x composites. This salt mixture not only helps in ordering and increasing the surface area of the material, but also acts as a source of zinc ions for *in situ* formation of ZnS during the carbonization process. On the other side, the use of 2-amino-4-phenyl thiazole as precursor serves as the single source for both N and S doping. Moreover, *in situ* synthesis leads to ZnS composites having good contact with the carbon matrix that helps in buffering the volume change of ZnS on lithiation/delithiation. This developed synthesis route has also the advantage to be simple, low cost, and high yield.

## 2. Experimental

### 2.1. Synthesis of the precursor for carbon material

The synthesis of 2-Amino-4-phenyl thiazole was carried out according to the procedure reported in the literature<sup>27</sup>. The reactants consisting of acetophenone (0.1 moles), iodine (0.1 moles) and thiourea (0.2 moles) were mixed in a ceramic mortar and the mixture was transferred to a 250 mL round bottom flask for heating at 110°C for 24 h. The reaction mixture was extracted with ether to remove the excess unreacted iodine and acetophenone. The residue from the aqueous layer was further dissolved in boiling water and on cooling; it was made alkaline using ammonium hydroxide solution. The obtained solid was filtered and washed multiple times with distilled water. Finally the separated solid was recrystallized in ethanol.

### 2.2. Synthesis of active materials

The carbon precursor (2-Amino-4-phenyl thiazole) was mixed with LiCl (23 mol %) /ZnCl<sub>2</sub> (77 mol %) in a 1:3 ratio. The dry mixing of precursor and salt mixture was done in a ceramic mortar with pestle. The well-ground mixture was transferred to the crucibles and carbonized at 800 and 900°C in a furnace at a heating rate of 5°C/min under Ar flow. The maximum temperature was held for 2 h. The materials prepared by carbonization followed by ball milling were further stirred with distilled water for 2-3 h; this mixture was filtered and subsequently washed with warm distilled water to get rid of excess salt or other side products. The resulting material was finally dried at 80°C for 1h.

### 2.3. Material characterization

To investigate the crystal structure, X-Ray diffraction (XRD) pattern was recorded with a powder diffractometer (D5000, Siemens; Cu-K<sub>α1, 2</sub> radiations) in the 2θ range between 15° and 80°. Nuclear magnetic resonance spectroscopy (NMR) was used for structural analysis of the synthesized precursor. The <sup>1</sup>H and <sup>13</sup>C NMR spectra were recorded on a Bruker spectrometer at 300 and 75 MHz respectively. The solvent used for NMR spectroscopy was DMSO-d<sub>6</sub>. The morphologies and other structural characteristics were investigated by field emission scanning electron microscopy (FESEM) (Supra 55,

Zeiss) with an accelerating voltage of 10 kV. For obtaining more detailed morphological and chemical information TEM/STEM measurements was conducted using a Tecnai F20 ST (FEI, Eindhoven, NL) with a field emission gun operated at 200 kV, equipped with an Orius SC600 CCD camera (Gatan, Pleasanton, CA) and an S-UTW EDX Si(Li) detector (EDAX, Mahwah, NJ). EDX line profiles were acquired in STEM-mode using drift correction, with a sample tilt of 20° towards the detector. Sample preparation was done by dispersing a spatula tip of the composite material in ethanol (grade p.a.). After sedimentation, one drop of solution was spread with a pipette onto 300 mesh TEM copper grids coated with lacey carbon film (Plano, article number S 166-3).

The thermogravimetric analysis was carried out through a thermogravimetric analyzer (Netzsch STA 490) in a temperature range 25°C to 900°C at a heating rate of 5°C/min in air. For specific surface area analysis N<sub>2</sub> sorption/desorption analysis was done on Micromeritics (Flowsorb II 2300). Measurement of the particle size distribution was carried out by laser scanning (Horiba LA950), Raman spectroscopy was performed by a Horiba LabRAM HR spectrometer. To study the surface composition, X-Ray photoelectron spectroscopy (XPS) was used. Measurements were performed using a K-Alpha+ instrument (Thermo Fisher Scientific, East Grinstead, UK), applying a 400 μm spot size of a monochromated Al Kα X-ray source. The spectra were fitted with Voigt profiles using the Thermo Avantage software. All spectra were referenced to the C 1s peak of hydrocarbon at 285.0 eV. The uncertainty of the binding energy is about ±0.1 eV for intense peaks and/or peaks clearly evidenced by the peak shape. On the other hand weak peaks for which no direct justification made by the peak shape, the uncertainty is ± 0.2 eV.

#### 2.4. Electrochemical characterization

The working electrodes were prepared by coating uniform slurry on a 10 μm thick copper foil (current collector). The components of the slurry were active material (86 wt. %), carbon black (Super C65, Imerys Graphite and Carbon, 6 wt. %), carboxymethyl cellulose (CMC, CRT2000, Dow Wolff Cellulosics, 6 wt. %) and styrene-butadiene (SBR) copolymer latex (TRD2001, JSR Corporation, 4 wt. %). All the components of the slurry were mixed in deionized water by a dissolver mixer (VMA Getzmann). For the preparation of bare ZnS working electrode, the electrode slurry with the same composition was used. The mass loading on each electrode was kept between 3-4 mg cm<sup>-2</sup>. Before assembling of the cells the punched electrodes (12 mm) were dried in a vacuum oven at 120 °C. Swagelok type cells with two electrodes were assembled in an Ar-filled glove box with lithium metal used as both counter and a reference electrode. A glass fiber foil (Whatman®-GF/D) was used as a separator and the electrolyte was BASF LP30 [1M LiPF<sub>6</sub> in ethylene carbonate/dimethyl carbonate (1:1, w/w)]. The electrolyte quantity was 80 μL in each cell. The capacity of composite anodes was calculated on the basis of the whole active material mass. Cyclic voltammetry (CV) and galvanostatic charge/discharge

experiments were carried out by an Arbin battery cycler (BT2000, Arbin Instruments). The CV was carried out in the potential range of 0.01-3.0 V vs Li/Li<sup>+</sup> at a scan rate of 0.1 mV s<sup>-1</sup>. CV with varying scan rates (0.1, 0.2, 0.4 and 0.6 mV s<sup>-1</sup>) was also performed. All the discharge/charge experiments were also performed in a potential range of 0.01-3.0V vs. Li/Li<sup>+</sup> with varying specific currents (25, 50, 100, 250, 500, 1000 and 1500 mA g<sup>-1</sup>). The discharge/charge experiments were also conducted with a current density of 250 mA g<sup>-1</sup> for long-term cycling. For electrochemical impedance spectroscopy (EIS), PAT-cells from EL-cells (Germany) were used. These cells were assembled with a Li disc as a counter electrode, a glass fiber separator, a Li-ring as a reference electrode and 150 μL of LP30 as the electrolyte. EIS was carried out in the frequency range 100 kHz – 10 mHz using a multichannel potentiostat (VMP3, Bio-Logic) with test cells inside a Binder climate chamber at 25 °C. The EIS were analyzed using Relaxis 3 software (rhd Instruments, Germany).

### 3. Results and discussion

#### 3.1. Structural analysis

The simple synthetic scheme of the composites is illustrated in Figure 1. The synthesis of a precursor (2-Amino-4-phenyl thiazole) is followed by the carbonization of its mixture with eutectic salt (LiCl/ZnCl<sub>2</sub>). The inbuilt N and S atoms of the precursor act as dopants during the carbonization process. However, the Zn<sup>2+</sup> ions from the eutectic salt mixture combine with the sulfur, liberated from the precursor during the carbonization and thus form *in situ* ZnS. The structure confirmation of the synthesized precursor was done by the H<sup>1</sup> and C<sup>13</sup> NMR as presented in Figure S1.

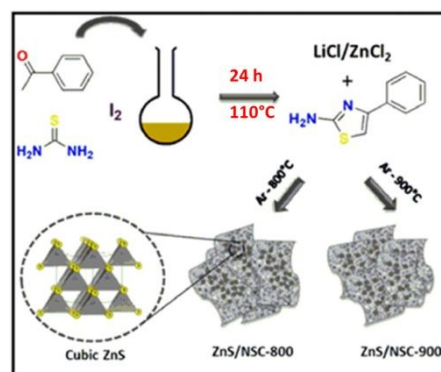


**Figure 1:** Schematic representation of the synthesis of ZnS/NSC-800 and ZnS/NSC-900

The synthesis and phase purity of *in-situ* synthesized ZnS is confirmed by XRD (Figure 2a). The peaks present at 2θ 28.5°, 47.6°, and 56.4° correspond to (111), (220) and (311) single phase crystal planes of cubic zinc sulfide structure<sup>8</sup>. The average crystal size of the synthesized composites calculated by the Debye Scherer equation from the most intense XRD peak was 9 nm. The diffraction peaks related to the heteroatom-doped carbon in composites cannot be observed, which displays the amorphous nature of the carbon matrix. In

addition, no peaks related to impurities are observed, which shows the purity of the synthesized composites.

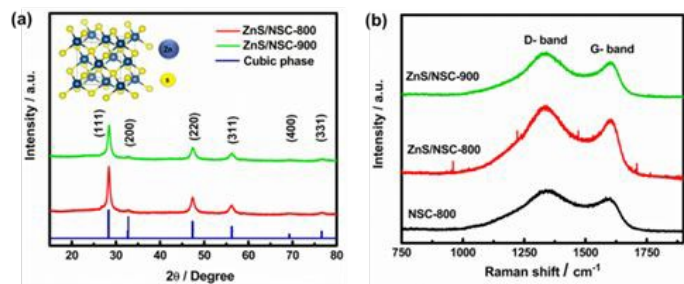


**Figure 2:** (a) XRD Diffraction patterns of ZnS/NSC-800 and ZnS/NSC-900 (b) Raman spectra of composites (ZnS/NSC-800, ZnS/NSC-900) and NSC-800

To further study the structure of carbon material in composites, Raman spectroscopy was carried out as presented in Figure 2b. The characteristic peaks arising at 1350 and 1590  $\text{cm}^{-1}$  were ascribed to D and G bands<sup>28</sup>. The D band arises from the deformation in the carbon matrix and the G band appears because of vibrations induced from the graphite-like carbon. The  $I_D/I_G$  value determines the degree of deformation in the carbon matrix, a higher value shows a higher deformation and less graphitization in the material<sup>28, 29</sup>. The extent of deformation induced by heteroatom doping by calculating  $I_D/I_G$  (see Table 1), decreases with the increase of the temperature. Moreover, the carbon material prepared without the use of salt mixture (NSC-800) show the smaller values for composites. This decrease of  $I_D/I_G$  with use of salt mixture indicates that the salt template has resulted in the formation of more ordered composites.

**Table 1:**  $I_D/I_G$  ratios obtained from Raman spectra

S. No	Sample	$I_D/I_G$
1	NSC-800	1.37
2	ZnS/NSC-800	1.24
3	ZnS/NSC-900	1.10

X-Ray photoelectron spectroscopy (XPS) was performed in order to study the heteroatoms doping and chemical bonding of elements in ZnS/NSC-x composites. The XPS survey spectra (Figure S2) show the presence of Zn, C, S, and N in the synthesized composites. The high-resolution Zn 2p spectra of ZnS/NSC-800 inserted in Figure 3(a) shows peaks at around 1044.8 eV and 1021.8 eV, which correspond to Zn 2p<sub>1/2</sub> and Zn 2p<sub>3/2</sub> peaks of ZnS. The presence of ZnS is further confirmed by the peak in the S 2p spectrum, with the characteristic binding energy at 161.5 eV<sup>18</sup>. The other two weak peaks at 163.5 eV and 167.9 eV are ascribed to C-S-C covalent bond and to C-SO<sub>x</sub>-C sulfone bridges respectively<sup>30, 31</sup>. To identify the nitrogen functionalities of ZnS/NSC-800, the N 1s peak was deconvoluted into three peaks with binding energies (398.1 eV), (399.9 eV) and (401.5 eV) which are assigned to pyridinic-N, pyrrolic-N, and quaternary N respectively (Figure 3b)<sup>32, 33</sup>.

In comparison to ZnS/NSC-800, the high magnification spectra of S 2p and N 1s for ZnS/NSC-900 (Figure 3c,d) show the smaller peak intensities, suggesting the decrease of nitrogen and sulfur content with increasing pyrolysis temperature<sup>34</sup>. Thus, the XPS analysis demonstrates the successful doping of N and S at the graphite edges. It is presumed that the electrical conductivity and lithium storage performance for the heteroatom doped composites will be improved because of the introduction of more electrochemically active sites and the additional defects introduced by dopants.

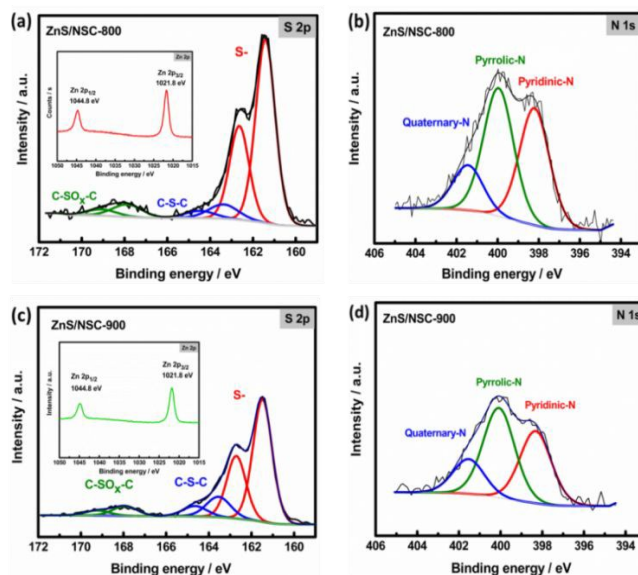


**Figure 3:** XPS. (a) Zn 2p and S 2p; (b) N 1s spectra of ZnS/NSC-800 and (c) Zn 2p and S 2p; (d) N 1s spectra of ZnS/NSC-900

The morphologies of the as-synthesized composites (ZnS/NSC-800 and ZnS/NSC-900) were investigated by Field emission scanning electron microscopy (FE-SEM), as presented in Figure 4. The high magnification SEM micrographs show that the particle size of ZnS/NSC-900 is finer than ZnS/NSC-800. Some graphitic sheets like morphology, in addition to globular structures, can also be observed in these materials. The cross-sectional SEM images of the composite electrodes in Figure S3 show ZnS particles well enclosed in the carbon layer. However, some of the nanocrystals were also found scattered on the surface of the carbon material. Moreover, the porosity, resulting from the use of salt mixture can also be seen in these images. The composites analyzed by EDX spectra shows the presence of Zn, S, C and N elements (Fig S4 h). The presence of embedded ZnS was also confirmed from the elemental mapping (Figure S4) and the existence of Zn and S peaks in 1:1 atomic ratio in the corresponding EDX spectra (Table S1).

Figure 4g shows a TEM bright field image, and from the same area a STEM HAADF image (Figure 4h) of ZnS/NSC-900, tilted 20° towards the EDX detector. In the TEM image, ZnS crystallites appear with dark contrast. They are partly agglomerated, in some cases single dark spots of around 10nm can be observed (see red arrow). The ZnS-crystallites are embedded in an amorphous appearing matrix. In STEM, the ZnS particles appear bright, whereas the carbon exhibits less contrast. The EDX line profile (location is the yellow line)

indicates clearly that STEM-signal intensity, Zn and S-intensity evolve in parallel (Figure S5). The HR-TEM image (Figure 4h) shows a ZnS particle, where (111) fringes with a distance of 0.31 nm corresponding to planes of ZnS crystals are visible. Around the particle, carbonaceous matrix can be detected.

Further, the particle size distribution of the two composites (Figure 5a) displays the decrease of particle size with the increase in pyrolysis temperature. The average particle size of ZnS/NSC-800 and ZnS/NSC-900 was found to be 3.9 and 2.8  $\mu\text{m}$ , respectively. The Brunauer–Emmett–Teller (BET) surface area was also determined by the  $\text{N}_2$  adsorption isotherm, as shown in Figure 5(b). These isotherms can be categorized as Type IV which is indicative of the presence of micropores and mesopores<sup>35</sup>. The measured surface areas for ZnS/NSC-800 and ZnS/NSC-900 were 131 and 156  $\text{m}^2/\text{g}$ , respectively, which signifies that the use of salt mixture has resulted into the composites with a good surface area, which can lead to more contact between the electrolyte and active material interface, thus facilitating the electrochemical reactions. The relatively higher surface area of ZnS/NSC-900 is the result of high-temperature treatment as mentioned before, which is also in correspondence with the particle size measurement<sup>36</sup>.

In order to calculate the percentage content of ZnS and carbon in composites, thermogravimetric analysis was carried out, as presented in Figure 6. The TGA shows the three-step weight loss for both composites. The weight loss from 25°C to 150°C

loss results from the loss of coordinated water and oxygen-containing groups in the samples. However, the major weight loss in the third step, from 400 to 800°C, is the result of both the combustion of carbon and oxidation of ZnS to ZnO [24]. The conversion of ZnS to ZnO was confirmed by the XRD of the TGA residue presented in Figure S5. As ZnS was fully converted to ZnO, the quantity of ZnS from ZnO was calculated by the following formula<sup>24, 37</sup>.

$$\text{ZnO}\% = W_{\text{ZnO}} / W_{\text{Total}}$$

$$\text{ZnS}\% = \text{ZnO}\% \times M_{\text{ZnS}} / M_{\text{ZnO}}$$

Where  $W_{\text{ZnO}}$  is the weight of ZnO,  $W_{\text{Total}}$  is the total weight of the composite while  $M_{\text{ZnS}}$  and  $M_{\text{ZnO}}$  are the molecular masses of ZnS and ZnO respectively. The content of ZnS determined by the above formula was 52 and 40.5% for ZnS/NSC-800 and ZnS/NSC-900, respectively. The relatively lower content of ZnS in the composite prepared at 900°C results from the more loss of heteroatoms and heteroatom based carbon fragments at higher temperatures.

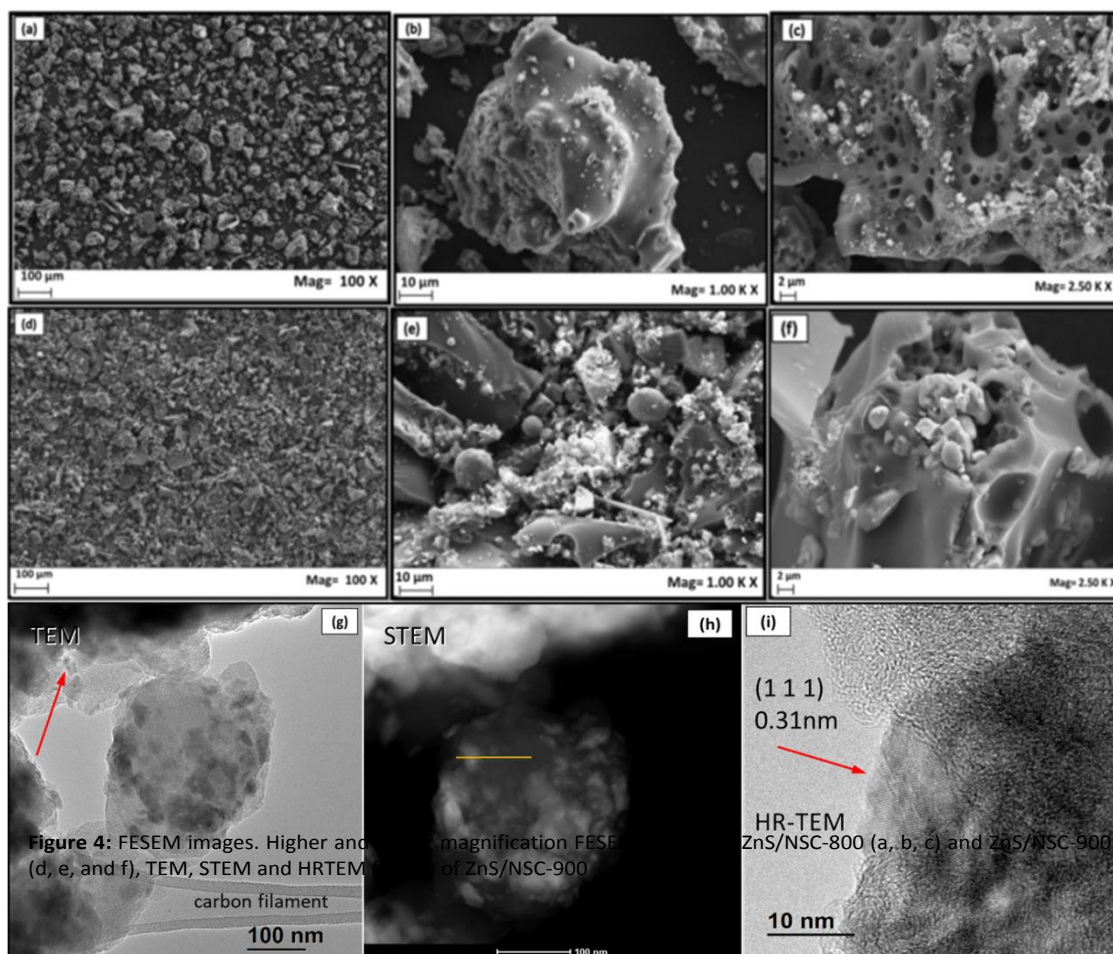


**Figure 4:** FESEM images. Higher and lower magnification FESEM images of ZnS/NSC-800 (a, b, c) and ZnS/NSC-900 (d, e, and f), TEM, STEM and HRTEM images of ZnS/NSC-900 (g, h, and i).

can be attributed to the adsorbed water. The second weight

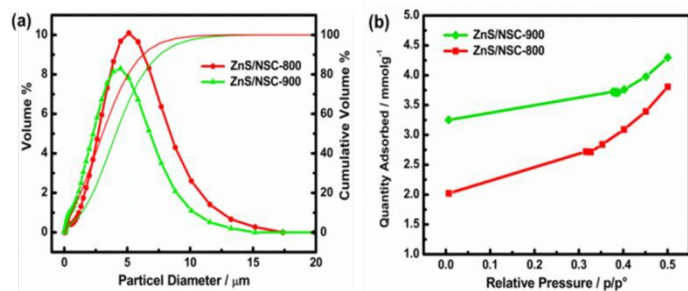


**Figure 5:** PSD and BET isotherms (a) Particle size distribution of the synthesized composites (b) N<sub>2</sub> adsorption isotherms of ZnS/NSC-800 and ZnS/NSC-900

### 3.2. Electrochemical characterization

To investigate the electrochemical behavior of the synthesized composites, cyclic voltammetry (CV) on bare ZnS and on the two composite electrodes was carried out. Figure S6 (a, b and c) shows the cyclic voltammogram of bare ZnS, ZnS/NSC-800 and ZnS/NSC-900 for the first four cycles. In the cathodic scan, several small reduction peaks appear below 0.8V, indicating the alloying and reduction of ZnS to metallic zinc in multiple steps. However, the small oxidation peaks, detected in the same potential range, represents the multistep dealloying of Li-Zn. A strong oxidation peak at 1.3V is attributed to the regeneration of ZnS from Zn. The CV curves are consistent with the previous literature<sup>38</sup>. However, the important point to note here is that the CV of bare ZnS is similar to the synthesized composites, but a rapid degradation can be observed. On the other side, the CV curves of both composites are well overlapped, showing the good electrochemical reversibility of the composite materials.

To further explore the electrochemical superiority of the composites, the uninterrupted rate performance was studied in half cells. Figure 7(a) shows the comparison of the rate performance of the composite materials (ZnS/NSC-800 and ZnS/NSC-900) with bare ZnS. The initial Coulombic efficiency of ZnS/NSC-800 is 74% however, only after a few cycles; this value becomes nearly 100%, which demonstrates the good electrochemical reversibility of the material. For ZnS/NSC-900 the relatively lower initial Coulombic efficiency (66%) is because of the comparatively higher surface area, which is responsible for large contact between the electrolyte-electrode interfaces, thus leading to more irreversible side reactions during SEI formation. However, after a few cycles, the Coulombic efficiency of ZnS/NSC-900 also becomes nearly 100%. Table 2 shows the specific capacities of the two composite electrodes and bare ZnS at various current densities. It can be seen that in comparison to the two composites, bare ZnS exhibits much lower capacities.

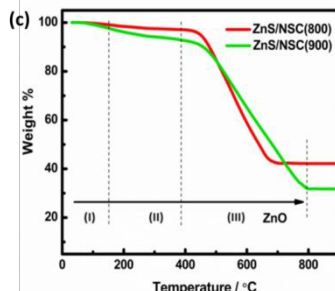


**Figure 6:** TGA curves of ZnS/NSC-800 and ZnS/NSC-900

Moreover, when the current density was again lowered to 250mA g<sup>-1</sup> after 46 cycles of cycling at various current densities, the reversible capacity of the composites can be recovered approximately to the initial capacities. By further lowering the current density to 25 mA g<sup>-1</sup>, about 84% of the initial capacity is recovered for ZnS/NSC-800. However, bare ZnS could only regain 53% of its initial capacity at the same current density. Hence, this also shows the structural stability of the composite electrodes even under high rate cycling.

**Table 2:** The specific discharge capacities of the two composite electrodes and bare ZnS at various current densities

S. No	Current densities (mA/g)	Specific discharge capacities (mAh/g)		
		Bare ZnS	ZnS/NSC-800	ZnS/NSC-900
1	25	898	895	960
2	50	459	586	577
3	100	320	508	490
4	250	208	429	370
5	500	114	357	286
6	1000	80	317	225
7	1500	60	279	200
8	250	205	403	360
9	25	241 (53%)	555 (84%)	534 (87)

The discharge/charge profiles of ZnS/NSC-800, ZnS/NSC-900, and bare ZnS at various current densities are presented in Figure 7(b, c, d). In these discharge/charge curves, the rapid capacity drop, from 898 to 60 mA h g<sup>-1</sup>, can be visibly seen in case of bare ZnS. Moreover, the capacity retention of ZnS/NSC-800 is 65% on increasing current density from 250 to 1500 mA g<sup>-1</sup>. The capacity retention of bare ZnS is only 28% which is much less than the one of the composites. This shows the excellent rate performance of the composites compared to bare ZnS. Among the two composites, ZnS/NSC-800 performs better with higher specific capacity and capacity retention with the subsequent increase in current densities. The possible explanation for the better rate performance of ZnS/NSC-800 is the presence of a relatively higher percentage of ZnS and more

dopants (N and S) that can also provide more electrochemically active sites and defects which are responsible for extra lithium storage.

View Article Online  
DOI: 10.1039/C9NJ02488C

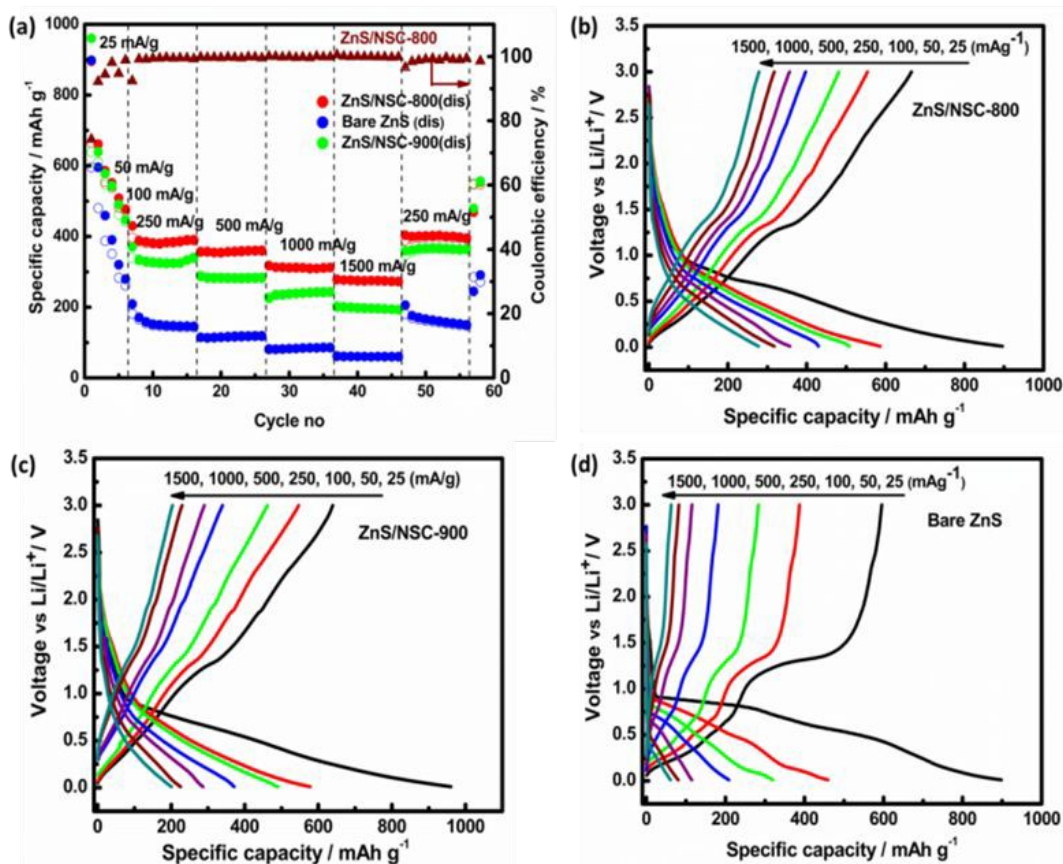


**Figure 7:** Uninterrupted rate performances and discharge/charge profiles. (a) Rate performance of bare ZnS, ZnS/NSC-800 and ZnS/NSC-900 (b, c, d) Discharge/Charge profiles of ZnS/NSC-800, ZnS/NSC-900, and bare ZnS respectively at different specific currents

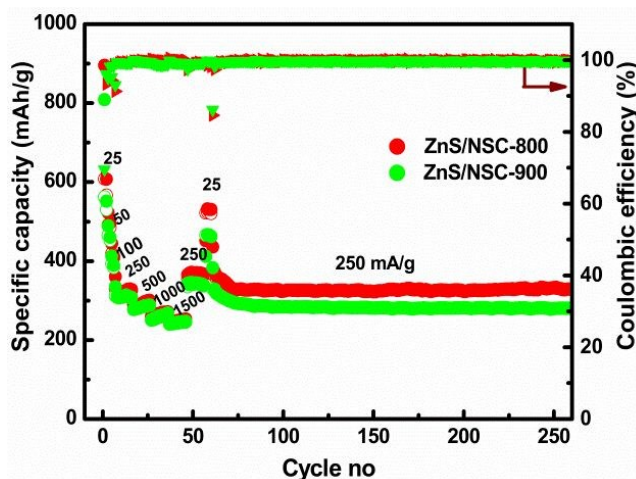


**Figure 8:** Cycling performance. Cycle performance at a current density of 250 mA g<sup>-1</sup> for 258 cycles

The cycling stability of the composite electrodes was also tested and compared with bare ZnS, as presented in Figure 8. The identical electrodes were used for both rate performance and cycling tests. The electrodes already cycled at various current densities were again discharged/charged at a current density of 250 mA g<sup>-1</sup> for about 200 cycles and the capacity retention for ZnS/NSC-800 is 90%. However bare ZnS retained only 31% of initial capacity after 200 cycles at same current density (see Figure S7). This result displays that the composite electrode already cycled under a stress environment of various current densities when subjected to further cycling, maintain good capacity retention that illustrates the good electrode structure integrity.

In order to study the reaction kinetics of the electrode materials and to have a better insight into the superior performance of composites, electrochemical impedance spectroscopy (EIS) was measured at different potentials. Figure 9(a) shows the Nyquist plots related to the composites and the bare ZnS at 1.3 V vs Li/Li<sup>+</sup>. These spectra can be fitted with the equivalent circuit shown in Figure 9(a). The resistance of separator, cell connections, and electrolyte (named R<sub>EL</sub>) is retrieved by the intercept with the real axis. At very high frequencies a small semicircle can be identified, which is related to the contact resistance and the resistance of the SEI (R<sub>s</sub>) and the associated capacitance (C<sub>s</sub>). At medium frequencies, a second semicircle represents the charge transfer resistance (R<sub>CT</sub>) and the related capacitance (CPE<sub>CT</sub>). This is followed by the solid diffusion in the particle bulk (Warburg impedance, W) and by the capacitance at very low frequencies (here named CPE<sub>3</sub>). The R<sub>CT</sub> of ZnS/NSC-800 is the smallest one among the three materials. On the other side, bare ZnS shows the highest R<sub>CT</sub>. The low R<sub>CT</sub> for composites imply that the heteroatom-doped carbon matrix is beneficial for the improvement of reaction kinetics. The resistance evolution from the Ohmic drop (as calculated from the charge/discharge curves of cycled electrode) also shows that after cycling the IR drop is much higher for ZnS than ZnS/NSC-x electrodes.

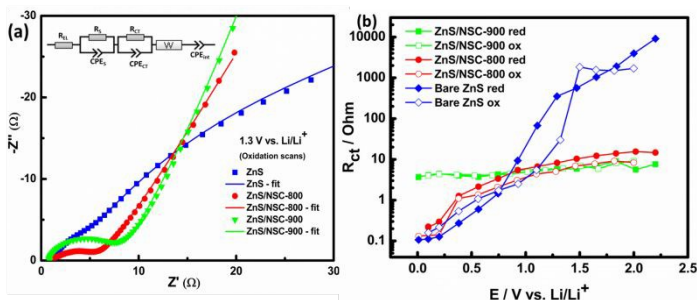


**Figure 9:** Electrochemical impedance results and R<sub>ct</sub> at various potentials. (a) Nyquist plots of Bare ZnS, composites and an equivalent circuit model for EIS (b) Comparison of charge transfer resistance at various potentials

Figure 9(b) shows the charge transfer resistance of the three electrodes at different potentials. It can be seen that the value of R<sub>ct</sub> related to the pure ZnS is smaller at low potentials and dramatically increases at higher potentials. The higher charge transfer resistance related to the composites at low potential can be explained by considering that Li insertion into carbon layers takes place at low potentials, giving rise to an additional

R<sub>CT</sub> (charge transfer into the graphitic carbon), which overlaps to the one of ZnS. Moreover, ZnS/NSC-900 shows higher charge transfer resistance at low potentials respect to both, ZnS/NSC-800 and bare ZnS. The higher graphitization degree in ZnS/NSC-900 leads to smaller interlayer distance, thus inducing sluggish intercalation. Hence, the decreased interlayer spacing can be the possible reason for the high charge transfer resistance of ZnS/NSC-900 at low potentials. The impedance measurements show that the *in situ* synthesized ZnS/NSC-800 has very low R<sub>ct</sub> which is beneficial for achieving improved kinetics. Moreover, with 50% of ZnS content and moderate surface area the storage capacities for ZnS/NSC-800 are comparable to the composites of higher surface area having larger ZnS content and low initial Coulombic efficiencies<sup>11, 12, 39</sup>.

### 3.3. Kinetic Analysis

To further have an understanding about the electrometrical performance, kinetic analysis through CV was performed. In this purpose, CV measurements at different scan rates were performed, as presented in Figure 10 (a, b). The charge storage process generally involves different mechanisms<sup>40</sup> and the broad categorization of the storage mechanisms can be done by the CV data obtained at different scan rates by using the following relation<sup>34</sup>:

$$i = av^b \quad (1)$$

$$\log(i) = b \log(v) + \log(a) \quad (2)$$

Where i represents the measured current density, v is the scan rate, while a, and b are the constants. A value of 0.5b indicates a pure diffusion-controlled (faradaic intercalation/insertion) process, whereas b=1.0 means a pure capacitive behavior<sup>41, 42</sup>.

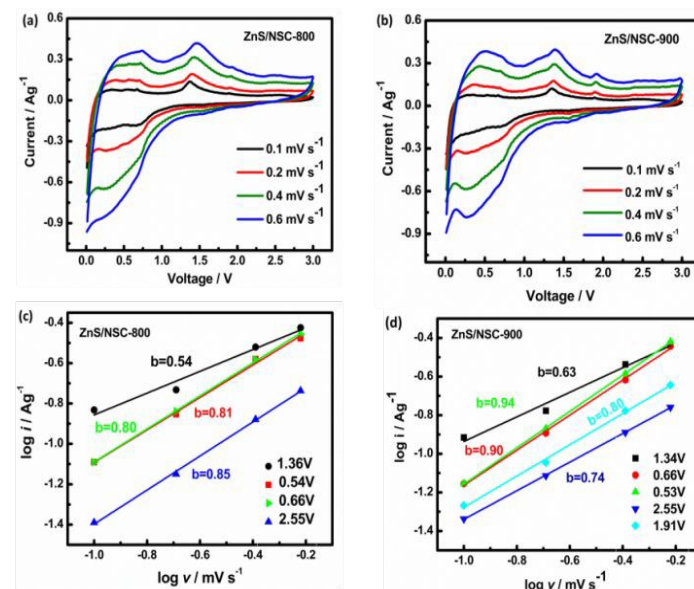


**Figure 10:** Multiscan cyclic voltammetry. (a, b) CV curves of ZnS/NSC-800 and ZnS/NSC-900 for LIBs ranging from 0.1 to 0.6 mV s<sup>-1</sup> (c, d) log(i) vs log(v) plots for calculation of b value

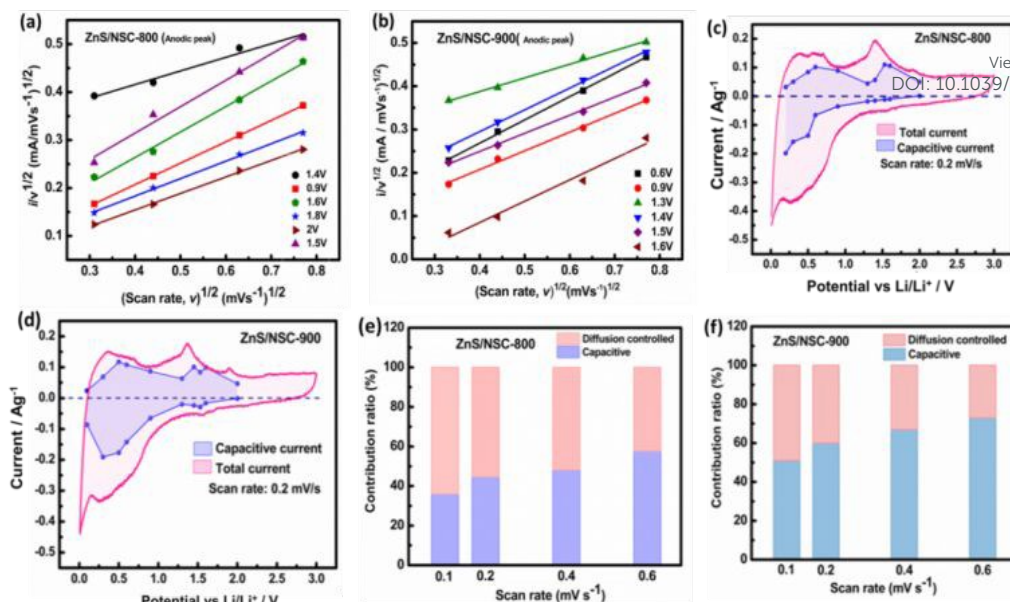


**Figure 11:** Quantification of capacitive current. (a, b)  $v^{1/2}$  versus  $i/v^{1/2}$  plots at various potentials used for calculating  $k_1$  and  $k_2$  (c, d) Contribution ratio of capacitive and diffusion-controlled capacities at a scan rate of  $0.2 \text{ mV s}^{-1}$  (e, f) Contribution ratio of capacitive current to Li storage at different scan rates ( $0.1\text{-}0.6 \text{ mV s}^{-1}$ )

To determine the b value for the synthesized composites at various potentials,  $\log i$  was plotted against  $\log v$ , as presented in Figure 10 (c, d). At 1.3V, the calculated b value of anodic peak is 0.54 for ZnS/NSC-800. However, for ZnS/NSC-900, the b value is 0.63. This higher b value indicates a predominance of diffusion controlled process with a slight surface capacitive contribution. The reason for the higher b value for ZnS/NSC-900 is the relatively higher carbon percentage and surface area, which can also contribute to the capacitive storage via a double layer mechanism. To further quantify the capacitive contribution in relation to the total stored capacity in ZnS/NSC-800 and ZnS/NSC-900, following relation was used<sup>34</sup>.

$$i(V) = k_1v + k_2v^{1/2} \quad (3)$$

By rearranging equation (3)

$$i(V)/v^{1/2} = k_1 v^{1/2} + k_2 \quad (4)$$

where  $k_1$  and  $k_2$  are constants for a given potential V. The  $k_1v$  represents the current contribution related to the capacitive process, while the  $k_2v^{1/2}$  represents the current contribution

due to the diffusion-controlled storage. The  $k_1$  and  $k_2$  values were obtained by plotting  $i(V)/v^{1/2}$  vs  $v^{1/2}$  as shown in Figure 11(a, b) where  $k_1$  is determined from the slope<sup>34, 43-45</sup>.

Figure 11 (c, d) shows the capacitive contribution (shaded blue) of synthesized composites (ZnS/NSC-800 and ZnS/NSC900) in relation to the total measured current at a scan rate of  $0.2 \text{ mV s}^{-1}$ . The higher percentage of capacitive current for ZnS/NSC-900 (60%) is the result of relatively higher surface area and carbon percentage as mentioned before. The quantification of capacitive current for other scan rates ( $0.1, 0.2, 0.4$  and  $0.6 \text{ mV s}^{-1}$ ) was also done as presented in Figure 11 (e, f). It can be seen that for ZnS/NSC-800, 44% of the total capacity is capacitive at a scan rate of  $0.2 \text{ mV s}^{-1}$  and it reaches

the 57% at a scan rate of  $0.6 \text{ mV s}^{-1}$ , which shows the dependence of capacitive current on scan rate. The higher capacitive contribution at high current densities leads to the good rate capability of these materials<sup>10</sup>.

## Conclusions

The two composites ZnS/NSC-800 and ZnS/NSC-900 were successfully synthesized with ZnS nanoparticles (9 nm) embedded into the carbon matrix *via* the salt templating method. The simple devised strategy of one step *in situ* synthesis produced ZnS nanoparticles well encapsulated into the N and S co-doped carbon matrix. The use of the salt mixture, besides providing zinc ions for the *in situ* formation of ZnS, also induces good surface area to the composites. The synthesized nanocomposites were used as a positive electrode for lithium-ion battery and they exhibit better rate performance and cycling stability than pure ZnS. Among the two composites, the storage capacities are higher for ZnS/NSC-800, with the initial specific capacity of  $895 \text{ mAh g}^{-1}$ . This can be attributed to the higher %age of ZnS and the relatively lower carbon percentage. Upon long repeated cycles, the pure ZnS displays a rapid degradation; while N and S co-doped carbon coated ZnS give stable capacities. Indeed ZnS/NSC-800 retains 90% of the initial capacity after 200 cycles. Besides the good cycling stability, the composites also show better rate performance in comparison to pure ZnS. The capacity retention of ZnS/NSC-800 is 65% on increasing current density from  $250$  to  $1500 \text{ mA g}^{-1}$ , while pure ZnS retains only 28% of its initial capacity at the same current densities. The better rate capability can be ascribed to the improved conductivity of the *in situ* synthesized composites. EIS analysis also shows the smallest charge transfer resistance for ZnS/NSC-800, thus further confirming the better electronic conductivity of composites. Moreover, the good cycling stability of the composites respect to the pure material shows that the carbon

coating also helps in buffering the volume change. This simple synthetic strategy can be easily applied to synthesize and explore also other composites in the future. Moreover, by the adjustment of heating rate and carbonization temperature, the quantity of ZnS in composites can be increased to more than 50% which can result in further high storage capacities.

### Conflicts of interest

There are no conflicts to declare.

### Acknowledgments

The authors acknowledge the scholarship funding by the Higher Education Commission of Pakistan under IRSIP program for this research. We acknowledge the support from Karlsruhe Nano Micro Facility (KNMF, [www.knmf.kit.edu](http://www.knmf.kit.edu)), a Helmholtz research infrastructure at Karlsruhe Institute of Technology (KIT, [www.kit.edu](http://www.kit.edu)). This work contributes to the research performed at CELEST (Centre for Electrochemical Energy Storage Ulm-Karlsruhe). The K-Alpha+ instrument was financially supported by the Federal Ministry of Economics and Technology on the basis of a decision by the German Bundestag.

### Notes and references

1. J. Cabana, L. Monconduit, D. Larcher and M. R. Palacin, *Advanced Materials*, 2010, **22**, E170-E192.
2. L. Fan, Y. Zhang, Q. Zhang, X. Wu, J. Cheng, N. Zhang, Y. Feng and K. Sun, *Small*, 2016, **12**, 5208-5216.
3. H. Li, Y. Wei, Y. Zhang, C. Zhang, G. Wang, Y. Zhao, F. Yin and Z. Bakenov, *Ceramics International*, 2016, **42**, 12371-12377.
4. H.-g. Wang, Y. Wang, Y. Li, Y. Wan and Q. Duan, *Carbon*, 2015, **82**, 116-123.
5. L. Lu, L. Jing, Z. Yang, G. Yang, C. Wang, J. Wang, H. Wang and Q. Jiang, *RSC Advances*, 2018, **8**, 9125-9133.
6. Y. S. Jang and Y. C. Kang, *Physical Chemistry Chemical Physics*, 2013, **15**, 16437-16441.
7. P. Li, Y. Liu, J. Liu, Z. Li, G. Wu and M. Wu, *Chemical Engineering Journal*, 2015, **271**, 173-179.
8. H. Du, X. Gui, R. Yang, H. Zhang, Z. Lin, B. Liang, W. Chen, H. Zhu and J. Chen, *Journal of Materials Science*, 2018, **53**, 14619-14628.
9. X. Zhu, D. Liu, D. Zheng, G. Wang, X. Huang, J. Harris, D. Qu and D. Qu, *Journal of Materials Chemistry A*, 2018.
10. J. Li, D. Yan, X. Zhang, S. Hou, T. Lu, Y. Yao and L. Pan, *Journal of Materials Chemistry A*, 2017, **5**, 20428-20438.
11. Y. Feng, Y. Zhang, Y. Wei, X. Song, Y. Fu and V. S. Battaglia, *Physical Chemistry Chemical Physics*, 2016, **18**, 30630-30642.
12. Y. Fu, Z. Zhang, X. Yang, Y. Gan and W. Chen, *RSC Advances*, 2015, **5**, 86941-86944.
13. R. Xie, Y. Li, H. Liu and B. Guo, *Journal of Alloys and Compounds*, 2016, **672**, 571-577.
14. Z. Zhu, S. Wang, J. Du, Q. Jin, T. Zhang, F. Cheng and J. Chen, *Nano letters*, 2013, **14**, 153-157.
15. F. Zhao, S. Shen, L. Cheng, L. Ma, J. Zhou, H. Ye, N. Han, T. Wu, Y. Li and J. Lu, *Nano letters*, 2017, **17**, 4137-4142.
16. J. Ma, X. Wang, H. Wang, G. Wang and S. Ma, *Journal of Alloys and Compounds*, 2018, **735**, 51-61.
17. Z. Chen, R. Wu, H. Wang, Y. Jiang, L. Jin, Y. Guo, Y. Song, F. Fang and D. Sun, *Chemical Engineering Journal*, 2017, **326**, 680-690.
18. H. Chen, B. Zhang, Y. Cao, X. Wang, Y. Yao, W. Yu, J. Zheng, J. Zhang and H. Tong, *Ceramics International*, 2018.
19. J. P. Paraknowitsch and A. Thomas, *Energy & Environmental Science*, 2013, **6**, 2839-2855.
20. L. Chen, X. Li, C. Ma, M. Wang and J. Zhou, *The Journal of Physical Chemistry C*, 2017, **121**, 18344-18350.
21. J. Liang, Y. Jiao, M. Jaroniec and S. Z. Qiao, *Angewandte Chemie International Edition*, 2012, **51**, 11496-11500.
22. Y. Qiao, M. Ma, Y. Liu, S. Li, Z. Lu, H. Yue, H. Dong, Z. Cao, Y. Yin and S. Yang, *Journal of Materials Chemistry A*, 2016, **4**, 15565-15574.
23. P. A. Denis, C. P. Huelmo and F. Iribarne, *Computational and Theoretical Chemistry*, 2014, **1049**, 13-19.
24. J. Li, Y. Fu, X. Shi, Z. Xu and Z. Zhang, *Chemistry–A European Journal*, 2017, **23**, 157-166.
25. X. Wang, J. Wang, D. Wang, S. Dou, Z. Ma, J. Wu, L. Tao, A. Shen, C. Ouyang and Q. Liu, *Chemical communications*, 2014, **50**, 4839-4842.
26. N. Fechner, T. P. Fellingner and M. Antonietti, *Advanced Materials*, 2013, **25**, 75-79.
27. P. Morales-Bonilla, A. Pérez-Cardeña, E. Quintero-Marmol, J. L. Arias-Tellez and G. J. Mena-Rejón, *Heteroatom Chemistry: An International Journal of Main Group Elements*, 2006, **17**, 254-260.
28. C. Yang, J. Xiong, X. Ou, C.-F. Wu, X. Xiong, J.-H. Wang, K. Huang and M. Liu, *Materials Today Energy*, 2018, **8**, 37-44.
29. J. Hou, C. Cao, F. Idrees and X. Ma, *ACS nano*, 2015, **9**, 2556-2564.
30. W. Li, M. Zhou, H. Li, K. Wang, S. Cheng and K. Jiang, *Energy & Environmental Science*, 2015, **8**, 2916-2921.
31. Z. Qiu, Y. Lin, H. Xin, P. Han, D. Li, B. Yang, P. Li, S. Ullah, H. Fan and C. Zhu, *Carbon*, 2018, **126**, 85-92.
32. F. Zheng, Y. Yang and Q. Chen, *Nature communications*, 2014, **5**, 5261.
33. T. Lin, I.-W. Chen, F. Liu, C. Yang, H. Bi, F. Xu and F. Huang, *Science*, 2015, **350**, 1508-1513.
34. W. Tian, H. Hu, Y. Wang, P. Li, J. Liu, J. Liu, X. Wang, X. Xu, Z. Li and Q. Zhao, *ACS nano*, 2018, **12**, 1990-2000.
35. K. Sing, D. Everett, R. Haul, L. Moscou, R. Pierotti, J. Rouquerol and T. Siemieniewska, in *Wiley Online Library*, 2008.
36. P. Fu, S. Hu, J. Xiang, L. Sun, S. Su and J. Wang, *Journal of Analytical and Applied Pyrolysis*, 2012, **98**, 177-183.
37. M. Jing, Z. Chen, Z. Li, F. Li, M. Chen, M. Zhou, B. He, L. Chen, Z. Hou and X. Chen, *ACS Applied Materials & Interfaces*, 2018, **10**, 704-712.
38. A.-R. Park, K.-J. Jeon and C.-M. Park, *Electrochimica Acta*, 2018, **265**, 107-114.
39. L. He, X.-Z. Liao, K. Yang, Y.-S. He, W. Wen and Z.-F. Ma, *Electrochimica Acta*, 2011, **56**, 1213-1218.
40. P. Yu, C. Li and X. Guo, *The Journal of Physical Chemistry C*, 2014, **118**, 10616-10624.

## Journal Name

## ARTICLE

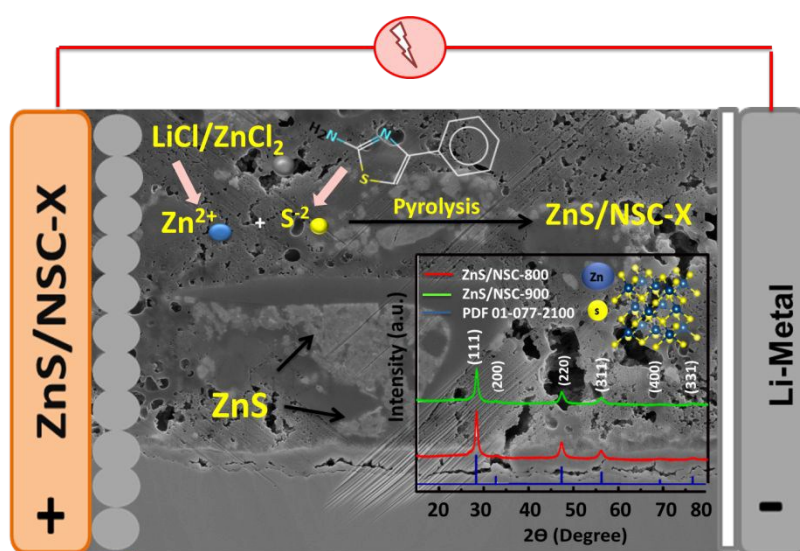
- 1  
2  
3 41. S. Dong, L. Shen, H. Li, P. Nie, Y. Zhu, Q. Sheng and X.  
4 Zhang, *Journal of Materials Chemistry A*, 2015, **3**, 21277-  
5 21283.  
6 42. E. Lim, C. Jo, H. Kim, M.-H. Kim, Y. Mun, J. Chun, Y. Ye, J.  
7 Hwang, K.-S. Ha and K. C. Roh, *ACS nano*, 2015, **9**, 7497-  
8 7505.  
9 43. Z. Chen, V. Augustyn, X. Jia, Q. Xiao, B. Dunn and Y. Lu,  
10 *ACS nano*, 2012, **6**, 4319-4327.  
11 44. Y. Wang, Y. Zhang, J. Shi, X. Kong, X. Cao, S. Liang, G. Cao  
12 and A. Pan, *Energy Storage Materials*, 2018.  
13 45. J. B. Cook, H. S. Kim, Y. Yan, J. S. Ko, S. Robbenolt, B.  
14 Dunn and S. H. Tolbert, *Advanced Energy Materials*, 2016,  
15 **6**, 1501937.  
16  
17  
18  
19  
20  
21  
22  
23  
24  
25  
26  
27  
28  
29  
30  
31  
32  
33  
34  
35  
36  
37  
38  
39  
40  
41  
42  
43  
44  
45  
46  
47  
48  
49  
50  
51  
52  
53  
54  
55  
56  
57  
58  
59  
60

View Article Online  
DOI: 10.1039/C9NJ02488C

New Journal of Chemistry Accepted Manuscript

## One step *in situ* synthesis of ZnS/N and S Co-doped Carbon Composites *via* salt templating for Lithium-ion battery application

Sadaf Ikram<sup>a,b</sup>, Marcus Müller<sup>b</sup>, Sonia Dsoke<sup>b,c</sup>, Usman Ali Rana<sup>d</sup>, Angelina Sarapulova<sup>b</sup>, Werner Bauer<sup>b\*</sup>, Humaira M. Siddiqi<sup>a\*</sup>, Dorothée Vinga Szabó<sup>b,e</sup>



### Entry for Table of Contents

Eutectic salt mixture (LiCl/ZnCl<sub>2</sub>) as a template plays a dual role by rendering sufficient surface area and a source of Zn<sup>2+</sup> for *in situ* formation of ZnS. Phenyl thiazole is a precursor for self-doped N and S carbon material. The resulting ZnS/ N and S Co-doped carbon composites as anode for Li-ion battery exhibit superior performance than pure ZnS.